Drift wave instability near a magnetic separatrix

J. R. Myra, D. A. D'Ippolito

Lodestar Research Corporation

X. Q. Xu

Lawrence Livermore National Laboratory

December 2001

DOE/ER/54392-16 LRC-01-85

LODESTAR RESEARCH CORPORATION

2400 Central Avenue

Boulder, Colorado 80301

Drift wave instability near a magnetic separatrix

J. R. Myra, D. A. D'Ippolito

Lodestar Research Corp., 2400 Central Ave. P-5, Boulder, Colorado 80301

X. Q. Xu

Lawrence Livermore National Laboratory, Livermore, CA 94550

Abstract

It is well known that the pure drift-Alfvén wave (DW) (i.e. in the absence of curvature and toroidal coupling effects) is stabilized by magnetic shear in circular flux surface geometry when the drift frequency is constant radially, [P.N. Guzdar, L. Chen, P.K. Kaw and C. Oberman, Phys. Rev. Lett **40**, 1566 (1978)] as is implicit in a local ballooning analysis. In the edge plasma near a magnetic separatrix, X-point geometry is important and the circular flux surface model does not apply. Using several numerical codes and analytical models, we find that the DW is robustly unstable in this case. Physically, instability is driven by wave reflection from the steep profile of $k_\perp$ near the X-points, due to magnetic shear and the local minimum of the poloidal magnetic field. It is concluded that a complete set of dimensionless parameters describing edge turbulence must include DW parameters that embody the physics of X-point effects and plasma shaping.

PACS: 52.35.Kt, 52.35.Bj, 52.55.Fa

I. Introduction

The drift-wave character of edge turbulence has long been of interest for magnetically confined, fusion-relevant plasmas, including the tokamak. Moreover, drift effects may be of special interest in low aspect ratio tokamaks and spherical tori, as a result of the low outboard magnetic field, relatively large Larmor radii, and large drift frequencies in the outboard edge plasma.

A great deal of work on drift waves has been reported in the literature, only a small fraction of which is cited in the following.[1-16] Much effort was directed towards an understanding of the "universal" drift instability in sheared systems, first in slab (or cylindrical) geometry and then in toroidal geometry. Because our present interest is in edge physics and the steep density gradient pedestal region, the papers which are most relevant employ a drift-Alfvén (drift-magnetohydrodynamic) model, where the drift frequency ω_* can be comparable to the Alfvén frequency $\omega_a = k_\| v_a$. Generally, the model must include dissipative (resistive) or electron inertial effects to obtain instability. In this paper, we consider the drift-Alfvén wave class of instabilities, hereafter referred to as drift-wave (DW) instabilities for brevity.

Early work employing local theory in shearless systems identified the basic DW instability drive mechanisms.[1-4] A body of literature dealing with the subtleties of drift instabilities in sheared slab (or equivalently a sheared cylinder or infinite aspect ratio torus) ultimately showed that the resistive drift-Alfvén mode was stable unless either toroidal curvature effects (entering at finite aspect ratio) or a ω_* profile with a maximum was considered.[5,6] The physics of shear damping and the role of toroidal effects on drift waves were explored in a series of papers.[7-9] The latter of these[9] even considered X-point effects, but not in the context of a drift-Alfvén model where the physics we are highlighting in the present paper could emerge. The drift-Alfvén equations remained a useful paradigm for plasma edge turbulence, enabling studies of turbulent cascades, and turbulence-induced diffusion in both shearless[4,10] and sheared[11-14] models of interest for both tokamaks and stellarators.[15] The possible role of the drift-Alfvén mode in the physics of the low-to-high confinement (L-H) transition has also been explored.[16] In a recent paper along these lines,[17] an equilibrium X-point effect was invoked in conjunction with drift-wave physics; however, the drift wave itself was treated in a shearless slab.

The full drift-resistive magnetohydrodynamic (DRMHD) model in an axisymmetric torus contains both the drift-Alfvén instabilities which we consider here, and the curvature-driven (ideal and resistive ballooning) modes on which we have focused in earlier papers.[18,19] The curvature-driven modes are relatively well understood, at least at a conceptual level. Typically *ideal* magnetohydrodynamic (MHD) instability sets in when a parameter $\alpha \sim \gamma_{mhd}^2 / \omega_a^2$ exceeds an order unity threshold. Here the curvature drive is characterized by $\gamma_{mhd}^2 \sim c_s^2 / (RL_n)$ where c_s is the sound speed, R the major radius of the torus and L_n the density (or pressure) gradient scale length. In the *resistive* magnetohydrodynamic model (RMHD), there is generally instability at sufficiently high mode numbers even when α is below the critical value for ideal instability. When ion finite Larmor radius and drift effects are retained, as in the full DRMHD model, resistive modes are suppressed when the parameter $\alpha_d \sim \omega_{*i} / \gamma_{mhd}$ exceeds a value of order unity. Here the relevant wavenumber $k_\perp$ to be employed in ω_{*i} is determined from balancing the resistive and ideal terms in the ballooning equation (viz. $\omega_\eta \gamma_{mhd} \sim \omega_a^2$). The relevance of the dimensionless parameters α and α_d can be deduced from simple linear physics considerations,[20] although it appears that they also play a fundamental role in the nonlinear evolution of turbulence,[21] and in the subsequent generation of sheared flows.[22]

While the concepts described in the preceding paragraph are most easily understood in the geometry of a large aspect ratio torus with circular flux surfaces, they are also relevant with some modification to the curvature-driven instabilities in divertor geometry near a magnetic separatrix. In previous work,[18,19] we showed that X-point geometry and resistive effects were synergistic for a class of curvature-driven modes, the resistive X-point (RX) modes. The strong magnetic shear and deep local minimum of the poloidal magnetic field near an X-point give rise to short scales lengths (high local $k_\perp$) for resistive ballooning modes, enhancing the effect of X-point resistivity. This has the effect of making resistive physics (and hence curvature-driven instability) important at much lower mode numbers than would otherwise be possible.

In the present paper we show that X-point geometry has an equally important, and more subtle, effect on the drift-Alfvén class of instabilities. As noted previously, it is now well known that the pure DW (*pure* meaning in the absence of curvature and toroidal coupling effects) is stabilized by magnetic shear in circular flux surface geometry when the drift frequency is constant radially.[5-8] For the radially localized ballooning modes that we consider in this paper, the radially constancy of ω_* is implicit. Thus we should, and do, find that our DRMHD model is stable in circular geometry when curvature effects

are suppressed. In contrast, the same model exhibits robustly unstable modes in divertor geometry.

One way of anticipating this result is to note that in a radial eigenmode analysis of DW instability in circular geometry the results tend to be sensitive to the physics near the rational surface defined by $k_{||} = (nq-m)/qR = 0$. Near a separatrix, the local safety factor (determined by the local field line pitch) $q_{loc} = q_{loc}(\psi, \theta)$ varies strongly along a field line, and consequently a well defined rational surface does not exist (or to be more precise, the $k_{||} = 0$ surface does not coincide with a flux surface). It is not surprising that this fundamentally changes the character of the drift wave.

The goal of our paper is to explore the physics basis for DW instability, and to lay the groundwork for understanding new dimensionless parameters for edge turbulence that take the flux surface geometry as well as relevant DW plasma parameters into account. Ultimately it is hoped that the results will provide a deeper understanding of the role of DW physics on resistive X-point (RX) modes when both curvature and DW drives are present and competitive.

To explore the physics of these modes, we will draw upon several numerical codes and analytical models, which are briefly summarized next. Our most complete numerical model is the global three-dimensional electromagnetic turbulence code BOUT[19] which follows the time evolution of the plasma instabilities through and beyond their linear growth phase. We also employ two linear eigenvalue codes which invoke the ballooning formalism. The BAL code[18] is a shooting code based on the second order (in $\nabla_{||}$) DRMHD Alfvén ballooning mode equation. The MBAL code, discussed here, is a matrix method eigenvalue solver that treats the more complete set of coupled Alfvén and sound waves. Our analytical models, described in Sec. IV, describe special cases for the dependence of $k_{\perp}$ along a field line, and include a two-region model and a power law model.

The plan of our paper is as follows. In Sec II we present the basic equations and review the underlying physics of drift-Alfvén wave instability in a shearless slab plasma. In Sec. III we show from numerical solutions of the equations in X-point geometry that DW instability persists. The cause of the instability is shown to be due to X-point effects. Section IV develops some simplified physics-based models which incorporate the main geometrical effects of the X-points and permit some insight into the driving mechanism. In Sec. V the role of the sound wave is considered. Our conclusions are given in Sec. VI.

Several details of the two-region model and the power law model are given in the Appendices.

II. Reduced DRMHD model and drift-Alfvén instability

A. Basic DRMHD equations

We begin with a standard reduced four-field model for DRMHD given by the equations of vorticity, electron continuity, Ohm's and Amperes laws, and total parallel momentum. The linearized set of equations takes the following form

$$\frac{\partial \phi_1}{\partial t} = -i\omega_{*i}\phi_1 - \frac{1}{K^2}\left(v_a \nabla_{\parallel} J_1 + i\omega_{\kappa} n_1\right) \tag{1}$$

$$\frac{\partial n_1}{\partial t} = -i\left(\omega_{*e} + \omega_{\kappa e}\right)\phi_1 + i\omega_{\kappa e} n_1 + v_a \nabla_{\parallel} J_1 - c_s B \nabla_{\parallel} \frac{u_1}{B} \tag{2}$$

$$\frac{\partial J_1}{\partial t} = -\frac{1}{1+H}\left[(\omega_{\eta} + i\omega_{*e})J_1 + K^2 v_a \nabla_{\parallel}(\phi_1 - n_1)\right] \tag{3}$$

$$\frac{\partial u_1}{\partial t} = -c_s(1+\tau)\nabla_{\parallel} n_1 + \mu_{\parallel}\nabla_{\parallel}^2 u_1 + i\omega_{\kappa i} u_1 + \frac{ic_s(1+\tau)\omega_{*e}}{v_a K^2} J_1 \tag{4}$$

where the perturbed field quantities are defined by

$$\phi_1 = \frac{e\delta\phi}{T_e} \tag{5}$$

$$n_1 = \frac{\delta n}{n} \tag{6}$$

$$J_1 = \frac{\delta J_{\parallel}}{n e v_a} \tag{7}$$

$$u_1 = \frac{\delta v_{\parallel}}{c_s} \tag{8}$$

It is also useful to define the perturbed quantity

$$\psi = \phi_1 - n_1 \tag{9}$$

Other notations are standard, in particular $K = k_{\perp}\rho_s, \rho_s = c_s/\Omega_i$, $c_s^2 = T_e/m_i$, $\tau = T_i/T_e$, $v_a^2 = B^2/4\pi n m_i$, $\omega_{\eta} = \eta_{\parallel} k_{\perp}^2 c^2/4\pi$, $\omega_{*e} = -(cT_e/neB)\mathbf{k}_{\perp}\cdot\mathbf{b}\times\nabla n$,

$\omega_{*i} = (cT_i / neB)\mathbf{k}_\perp \cdot \mathbf{b} \times \nabla n$, $H = k_\perp^2 c^2 / \omega_{pe}^2$, $\omega_{\kappa e} = (2cT_e / eB)\mathbf{k}_\perp \cdot \mathbf{b} \times \kappa$,
$\omega_{\kappa i} = (2cT_i / eB)\mathbf{k}_\perp \cdot \mathbf{b} \times \kappa$, and $\omega_\kappa = \omega_{\kappa e} + \omega_{\kappa i}$, $\mu_\parallel = 1.92 v_i^2 / \nu_{ii}$.

The MBAL code solves Eqs. (1) – (4) in full, while the BAL code neglects u_1 to obtain a second order differential equation along the field lines. Various further approximations are shown to be useful in highlighting the underlying physics of the DW instability in X-point geometry. Throughout this paper, we shall neglect the curvature terms ω_κ, $\omega_{\kappa e}$ and $\omega_{\kappa i}$ to highlight the role of drift-driven, as opposed to curvature-driven, instabilities.

B. Drift-Alfvén instability in a shearless slab

The well known dispersion relation for the drift-Alfvén instability in a shearless slab may be derived from Eq. (1) – (4). It is convenient for later use to construct coupled equations for $\phi = \phi_1$ and ψ

$$\frac{\omega_a^2}{G}\psi = \omega\phi \tag{10}$$

$$[\omega^2(1+K^2) - \omega\hat{\omega}_{*e} - \hat{\omega}_s^2]\phi = (\omega^2 - \hat{\omega}_s^2)\psi \tag{11}$$

where

$$G = \omega(1+H) + i\omega_\eta - \omega_{*e} \rightarrow \omega H \tag{12}$$

$\omega_a = k_\parallel v_a$, $\omega_s = k_\parallel c_s$, $\hat{\omega}_s^2 = (1+\tau)\omega_s^2$, $\hat{\omega}_{*e} = \omega_{*e}(1-\beta)$, $\beta = \hat{\omega}_s^2 / \omega_a^2$ and the final form for G in Eq. (12) is the collisionless electrostatic limit. Here we have neglected ω_{*i} for simplicity, since it does not play a major conceptual role for this instability.

We note that when the square bracket on the left-hand-side of Eq. (11) vanishes, ϕ becomes singular. Later when we consider the ballooning equation generalization of Eq. (11) this singularity will occur at isolated points along the field line when ω_s is neglected and ω approaches the real axis.

The dispersion relation for drift-Alfvén modes is

$$\left(1 + K^2 - \frac{\hat{\omega}_{*e}}{\omega} - \frac{\hat{\omega}_s^2}{\omega^2}\right)\frac{\omega_a^2}{\omega G} = 1 - \frac{\hat{\omega}_s^2}{\omega^2} \tag{13}$$

which is fourth order in ω. The bracket on the left-hand-side together with the right-hand side provides a low frequency sound wave, and the drift wave (or if $\omega_{*e} = 0$, the two

sound waves), and the remaining factors provide the two Alfvén waves (e.g. in the ideal MHD limit where $G \rightarrow \omega$ and K, $\omega_{*e} \rightarrow 0$).

Figure 1 shows the dispersion plot corresponding to the collisionless electrostatic cold ion limit of Eq. (13) for an illustrative set of edge parameters (B = 5 kG, B_θ = 2 kG, R = 100 cm, T_e = 120 eV, $n_e = 3.5 \times 10^{12}$ cm^{-3}, L_n = 0.75 cm). Instability results from the coupling of the drift and Alfvén branches. Neglecting ω_s, the dispersion relation may also be rewritten to highlight the drift and Alfvén wave mode crossing as

$$(\omega + \omega K^2 - \omega_{*e})(\omega^2 - \omega_a^2) = -\omega^2(\omega H + i\omega_\eta - \omega K^2)\,. \qquad (14)$$

At mode crossing, when $\omega_a = \omega_{*e}/(1+K^2) \equiv \omega + \delta\omega$, one can expand the above form for small $\delta\omega$ to show the destabilizing effects of resistivity (ω_η) and electron inertia (H) and the stabilizing effects of polarization drift [K or $\beta = (m_e/m_i)(K^2/H)$].[1,2,16]

While the basic character of this instability in shearless slab geometry is modified in an essential way by magnetic shear in the circular flux surface tokamak model, we will see that it again becomes relevant when X-point effects are taken into account.

III. DW in X-point geometry

A. BOUT code results

BOUT code modeling of similar plasmas in circular flux surface and X-point geometry provides dramatic evidence of the role of the X-point effects. Results for the time evolution of a simulation initiated at noise levels is shown for the two cases in Fig. 2. For the circular flux surface Continuous Current Tokamak (CCT)[23] plasma (using illustrative parameters at the top of the edge pedestal: $T_e = T_i$ = 47.2 eV, $n_e = 4.93 \times 10^{12}$ cm^{-3}, B = 2.6 kG, R = 148 cm, a = 36 cm, q = 3, s = 2, and peak gradients $L_n = L_T$ = 3.0 cm at Ψ = 98%) the simulation remains at noise levels. In contrast the divertor geometry National Spherical Torus Experiment (NSTX)[24] plasma (using illustrative parameters at the top of the edge pedestal: $T_e = T_i$ = 53.4 eV, $n_e = 4.58 \times 10^{12}$ cm^{-3}, B_{a0} = 2.6 kG at the outboard midplane, R = 154 cm, a_0 = 46 cm, q_{95} = 3.2, and peak gradients $L_n = L_T$ = 2.5 cm at Ψ = 98%) shows the exponential mode growth of a strong linear instability. In these BOUT code runs, as in all results for this paper, curvature terms are suppressed to highlight the drift wave physics.

B. BAL code results

To understand the BOUT code results and elucidate the DW physics, we have performed a number of BAL code runs. The goal has been to isolate the crucial physics for DW instability, so that the role of geometry can be explored in the simplest possible physics model. The BAL code confirms robust instability only in divertor geometry.

Sample runs for an NSTX double null geometry (using the illustrative base case parameters given in Sec. II) compare the unstable spectra for three physics models in Fig. 3: the full electromagnetic model, the electrostatic limit, and the electromagnetic model with the collisionless skin term H artificially suppressed. Results show that instability for these parameters (which imply $\omega \sim \omega_{*e} > \nu_e$) is driven mainly by the collisionless skin term and the electromagnetic character of the mode is not critical. The real frequency of the mode (not shown in the figure) is of order ω_{*e}.

The low-n feature of the spectrum seen in Fig. 3 may be related to the "coherent mode" seen in some BOUT turbulence simulations[25] for Alcator C-Mod.[26] and NSTX. For the NSTX case that we have checked, the BOUT coherent mode and the low-n BAL code feature have similar perpendicular wavenumbers and oscillation frequencies. A series of BAL code runs indicate the dominant scaling of this feature with parameters. Instability is strongest at low T_i, high T_e small L_n and high q. Stronger drive correlates with the spectrum peaking at lower n. The q scaling is particularly strong, and is illustrated in Fig. 4. Depending on parameters the mode can be collisionless or collisional, as for the slab drift-Alfvén instability. The competition between the destabilizing skin effect and the stabilizing polarization drift results in a peak at a particular n.

The above studies are useful in guiding us to the simplest physics model in which DW instability exists. Using this reduced model will then permit an exploration of why and how the X-point geometry matters. A suitable reduced model is the electrostatic, collisionless limit with $T_i = 0$. In this model, the ballooning equation reduces to

$$B(\omega + \omega K^2 - \omega_{*e}) \frac{v_a^2}{H\omega} \nabla_{\|} \frac{1}{B} \nabla_{\|} \psi + \omega^2 \psi = 0 \qquad (15)$$

It is instructive to examine the structure, along the field line, of an unstable eigenmode of this equation. A typical example is shown in Fig. 5 where the X-points are located at $\theta = 0$ and 4 and $0 < \theta < 4$ corresponds to the outboard midplane of this double null configuration. Here θ is the usual extended ballooning coordinate. Several features

are noteworthy. The height of the eigenfunction in the outboard midplane region is large indicating the instability drive region is here, and that mode is flat in this region and has a standing-wave character. For large positive or negative θ, there is a clear outgoing wave structure. The jaggedness of the mode results from successive interactions with the X-points (and is not indicative of the scale of the numerical resolution which exceeds plotting accuracy).

By examining the variation of the quantity

$$\Lambda = 1 + K^2 - \omega_{*e} / \omega \tag{16}$$

along the field line (not shown) it is found that Re(Λ) changes sign near the X-points, being negative in the region $0 < \theta < 4$ and otherwise positive. $Re(\Lambda) < 0$ corresponds to a "negative energy" drift wave, [heuristically, from Eq. (15), $\delta W \propto \Lambda |\nabla_{||} \psi|^2$] thus confirming the location of the instability drive region. The point $\Lambda = 0$ is a singular point of Eq. (15), which will be discussed in more detail in Sec. V. For a robustly growing mode, the singular point is far off the Re(θ) axis.

The preceding analysis is a guide to the minimal set of physical equations that describe DW instability, but it does not lend much insight into the role of geometry. Why is the infinite aspect ratio circular plasma stable while the X-point plasma is unstable? Examining the terms of Eq. (15), the differences between the circle and X-point geometry cases can be categorized as: i) θ variations of B and R (not present in the infinite aspect ratio circular flux surface limit), ii) field line lingering near the X-point (i.e. θ variation of the Jacobian relating d/dθ and $\nabla_{||}$) and iii) X-point effects on the K(θ) profile (i.e. variations of magnetic shear and B_θ). Point i), the θ variations of B and R, is really a toroidal coupling effect, which is well known to lead to drift-wave instability;[7,8] thus we concentrate on the other two X-point related effects.

The runs summarized in Fig. 6 explore some artificial, but instructive, numerical tests. They indicate that instabilities result when either effect ii) or iii) is added to the circular flux surface geometry model. Thus, the circular model represents a mathematically unique limit and a very special case for pure DW stability: stability results can be sensitive to small changes from a pure circular model.

IV. Simplified physics-based models

A. Two-region model with Born matching

The analysis of the DW eigenfunction shown in Fig. 5 suggests that a very simple physics-based conceptual model might be useful in understanding more transparently how X-point geometry supports unstable modes. The physics is essentially that of the Hasegawa-Wakatani model[4] extended to include electron inertia and a simple geometric model for X-point magnetic shear.

We consider two regions along the field line $0 < \theta < \infty$ for an even parity mode. Region one for Eq. (15) is defined by $K << 1$ and is the drive region for instability. In this region we let

$$\psi = \cos k_{\|1} z, \qquad 0 < z < L \tag{17}$$

where z is distance along the magnetic field. The local uniform plasma dispersion relation in region one relates ω to $k_\perp$ and $k_{\|1}$

$$\omega_{a1}^2(\omega - \omega_{*e}) = H\omega^3 \tag{18}$$

Similarly, region two is defined by $K \to \infty$ and corresponds to the outgoing wave region. In this region we let

$$\psi = A_2 \exp[ik_{\|2}(z - L)], \qquad L < z < \infty \tag{19}$$

with local dispersion relation

$$\omega^2 = \omega_{a2}^2 K^2 / H \equiv \omega_e^2 \tag{20}$$

In the above $\omega_a = k_\| v_a$ and $\omega_e = k_\| v_e$ where v_a and v_e are the Alfvén and electron thermal velocities.

The two regions are matched together by a jump condition applied at z = L where L is a parallel scale length (typically of order R on field lines near the separatrix). If we were to neglect the pole contribution arising from Λ [see Eq. (16)] the jump condition from Eq. (15) is just continuity of ψ and $\nabla_\|\psi$. More generally, we obtain

$$\left[\nabla_\| \psi\right]_-^+ = Q\psi\,, \tag{21}$$

where it is shown in Appendix A using a Born approximation (ψ constant across the matching region) that

$$QL = -\xi^2\left(\frac{L_t}{L} - i\pi\frac{L_K}{L}\right), \tag{22}$$

where $L_K^{-1} = K^{-1}dK/dz$ and L_t is the length of the matching region. Here we have also defined $\xi = \omega L/v_e$. For validity of the two-region model $L_t/L << 1$ is required.

Combining Eqs. (17) – (21) we obtain the following coupled equations for the global eigenvalue $\xi \propto \omega$

$$x \tan x = -i\xi + QL \tag{23}$$

$$x^2(\xi - \xi_*) = K_0^2\xi^3 \tag{24}$$

where $x = k_{\|1}L$, $\xi = \omega L/v_e = k_{\|2}L$, $\xi_* = \omega_{*e}L/v_e = K_0/\lambda$, $\lambda = (m_i/m_e)^{1/2}L_n/L$ and K_0 is the value of K in region 1 (corresponding to $k_\theta\rho_s$ at the outboard midplane).

Analytical solutions of this eigenvalue equation are possible in many limiting cases. Details are given in Appendix B. One important limit that qualitatively reproduces the results of the BAL code is as follows. We neglect Q, expand the tan function for $\xi << 1$ and consider $K_0 << \lambda^{1/2}$ to obtain Re $\xi \sim K_0/\lambda$ and Im $\xi \sim K_0^4/\lambda^2$. Thus in dimensional variables the mode has a real frequency of order ω_{*e} and a growth rate $\gamma << \omega_{*e}$. The mode is flat between X-points because $\xi << 1$ implies $x = k_{\|1}L << 1$.

The pole contribution adds a damping term proportional to $i\pi L_K$ in Eq. (22) that generally reduces the growth rates. If the two-region model is taken to model X-point geometry, then L_K/L is a small parameter because, in the X-point region where the pole is to be evaluated, the strong magnetic shear makes L_K very short. We speculate from this qualitative argument that the larger order unity size of L_K/L in circular flux surface geometry may heuristically explain the stability of the DW in that limit. This point will be discussed further in connection with Fig. 7.

The two region model permits an evaluation of the ratio of transmitted (outgoing) wave to the standing wave amplitude, viz. ψ at the transition boundary z = L. This ratio is just sec ξ. The net growth of the drift wave is determined by balancing the instability drive with the outgoing wave energy loss. The amount of reflection at the X-point (here the z = L boundary) determines this balance.

B. Power law model

While the two-region model is conceptually useful, it does not permit a rigorous connection between X-point and circular geometry to be made. To accomplish this we consider a power law model for the K(θ) profile.

Our starting point for this model is the collisionless electrostatic eigenmode equation written in dimensionless variables

$$(1+K^2-\xi_*/\xi)\frac{\partial^2\psi}{\partial\theta^2}+K^2\xi^2\psi=0\,. \tag{25}$$

Here, $\xi = \omega/\omega_e$, $\xi_* = \omega_{*e}/\omega_e = K_0/\lambda$ where in analogy to the notation of the two-region model $\lambda = L_n/(qR\mu_e^{1/2})$, $\mu_e = m_e/m_i$ and $\omega_e = v_e/qR$. For this model, we consider the family of K profiles given by

$$K^2 = K_0^2[1+(s\theta)^\nu] \tag{26}$$

so that $\nu = 2$ corresponds to the standard circular flux surface model, and larger ν yields steeper profiles which can mock up X-point effects. A comparison of K(θ) profiles for an NSTX double dull case and Eq. (26) is given in Fig. 7a. Note that the power law model gives a good fit in the drive and transition regions. The power law model is not correct asymptotically for large K when $\nu \neq 2$, but this is of little consequence as the eigenmode equation is independent of K in this asymptotic regime. Figure 7b compares the inverse ratio of scales lengths L/L_K that appears in Eq. (22) and controls the strength of damping from the pole contribution. The value of L/L_K is only important at the pole, $\Lambda = 0$. In divertor geometry, the system can find an eigenvalue such that the pole is located where L/L_K is large (giving weak damping) while in circular geometry L/L_K is evidently never large enough to permit instability.

When ν is varied and the eigenvalue problem given by Eq. (25) is solved, we can continuously track the growth rates from zero at $\nu = 2$ to the asymptotic limit of the two-region model when $\nu \to \infty$. Results are shown in Fig. 8. The relation between the $\nu \to \infty$ limit and the two-region model is given in Appendix C.

Again, the results show that the circular plasma case is special. The collisionless electrostatic model in circular geometry is marginally stable, and thus susceptible to instability or over-stability by the addition of small effects. For example, we have shown that the collisional electromagnetic model in circular geometry is over-stable (not shown). However, for ν greater than a critical value, robust instability generally results. We

interpret the instability as resulting from reflections of the outgoing wave by the steep gradients in the K(θ) profile.

V. Role of the sound wave

So far, we have not considered the role of the sound wave in detail. In this section we show that explicitly including the sound wave in the model does not change our conclusion that the DW is stable in circular geometry but unstable in X-point geometry.

As alluded to in the preceding discussion, the singular point given by $\Lambda = 0$ in Eqs. (15) and (16) physically represents damping due to a mode conversion of the Alfvén wave to a sound wave. Treating the singular point as a pole (as occurs when ω_s is neglected in the model) retains the physics of sound wave damping, but cannot describe the sound wave propagation. To retain sound wave propagation, we employ the MBAL code which solves Eqs. (1) – (4) by matrix methods.

The MBAL code discretizes the parallel derivatives by employing a spectral decomposition. This results in a standard eigenvalue problem for a large, full, non-symmetric complex matrix which is solved by a commercially available package. The use of a non-uniform grid enables resolution of the fine structure of the sound wave near the mode-conversion point.

We have employed the MBAL code to study the effect of retaining the parallel velocity u_1. In general u_1 has little effect on the growth rates in either the circular plasma or X-point cases. The qualitative effect on the eigenfunction is most dramatic in the circular plasma case, where the growth rate theoretically tends to zero and the singular point $\Lambda = 0$ occurs on the real θ axis. In practice, this limit is exceedingly difficult numerically. Small reflections from the numerical box boundaries at large θ give rise to small but finite growth rates in the circular plasma limit. An example is shown in Fig. 9 where the potential ϕ_1 is shown with the sound wave suppressed and with it retained. The singularity in ϕ_1 is evident in Fig. 9 a). When u_1 (hence the sound wave) is retained in Fig. 9 b) the singularity is resolved and the sound wave propagation and damping is evident. For these cases the growth rate is the same to within numerical errors, and the real frequency differs by about 20%.

VI. Conclusions

We have shown that the pure drift-Alfvén wave (in the absence of curvature and toroidal coupling effects) is robustly unstable in X-point geometry even though it is stable in circular flux surface geometry. Physically, instability is enabled by reflections of the waves from the X-point regions as they propagate along the field lines. The reflections are caused by the steep $k_\perp(\theta)$ profile that arises due to both strong X-point magnetic shear and the local zero of B_θ. When these reflections occur at both upper and lower X-points (e.g. in a double null configuration) a partial standing wave forms between X-points on the outboard edge, and is susceptible to drift-Alfvén instabilities that have the same basic character as in a shearless slab configuration. Depending on parameters, the familiar collisionless (electron inertia driven) and collisional (resistivity driven) versions of the instability occur. Growth rates are generally weaker in realistic divertor geometry than for an equivalent shearless slab because the realistic geometry allows for partial transmission of wave energy through the X-point region where it becomes outgoing energy flux that damps the mode.

The present work can be thought of as building most directly on Ref. 5 since we investigate the stability of the drift-Alfvén modes in a similar physics model. (We extended it only slightly to include electron inertia giving rise to the collisionless skin terms.) Instead of studying the radial profile effects of $\omega_*(r)$ from a radial eigenvalue analysis, or examining toroidal coupling and curvature effects, we considered the effect of X-point geometry in a ballooning analysis along the field lines, implicitly taking $\omega_*(r)$ constant. Since we find that this model is sufficient to give rise to drift-Alfvén instability, it is tempting to speculate that *any* poloidal modulation of B or shear can allow instability in a drift wave system whether it is due to toroidal effects or poloidal geometry (shaping or X-points). However, not surprisingly as we have seen, the effect of X-points is particularly pronounced.

As a result, *divertor geometry* introduces a new drive for drift-wave instability that can contribute to edge turbulence together with the curvature drive that has been previously investigated for resistive X-point modes. A characterization of the relevant dimensionless drift parameters will be an important topic for future work; however, it is clear from the present paper that they must embody the physics of reflection due to X-points and flux surface shaping, and must vanish in the cylindrical plasma limit.

Acknowledgments

The authors wish to thank the NSTX team for providing magnetic geometry data, G.R Tynan for CCT parameters, and R.H. Cohen and W.M. Nevins for physics discussions. This work was supported by U.S. Department of Energy (DOE) under grant DE-FG03-97ER54392 and contract W-7405-ENG-48; however, such support does not constitute an endorsement by the DOE of the views expressed herein.

Appendix A: Pole contributions in the two-region model

In this appendix, we consider a rigorous derivation of the matching condition between the two regions of the model considered in Sec. IV A. In particular, we present the derivation of Eqs. (23) and (24) with the pole contribution QL given by Eq. (22).

In general, the jump condition between the two regions is given by integrating Eq. (15) across the transition between regions one and two, *viz.*

$$\left[\frac{1}{B}\nabla_{\|}\psi\right]_{-}^{+} = -\int\frac{dz}{B}\frac{H\omega^{3}\psi}{(\omega+\omega K^{2}-\omega_{*e})v_{a}^{2}} \tag{A1}$$

where dz is the increment of field line length measured parallel to **B**. Concentrating on the pole contributions, we neglect the variation of v_a, B and ψ so that they may be pulled through the integral (the Born approximation). This yields the result

$$\left[\nabla_{\|}\psi\right]_{-}^{+} = Q\psi\,, \tag{A2}$$

with

$$Q = -\frac{\omega^{2}}{v_{e}^{2}}\int dz\frac{\omega K^{2}}{\omega+\omega K^{2}-\omega_{*e}} = -\frac{\omega^{2}}{v_{e}^{2}}\int dz\left(1-\frac{\omega-\omega_{*e}}{\omega+\omega K^{2}-\omega_{*e}}\right) \tag{A3}$$

The first term in the final form for Q gives rise to the L_t term in Eq. (22), where L_t is the length of the transition region. In the remaining term, the limits of integration may be extended to $\pm\infty$ because the rapid growth of K^2 allows the contour to be closed in the lower half of the complex z plane when Im $\omega > 0$. The residue is evaluated by expanding about the pole $z = z_p$

$$K(z) = K_{p} + (z-z_{p})K_{p}'\,, \tag{A4}$$

to obtain

$$\int \frac{dz}{\omega + \omega K^2 - \omega_{*e}} = -\frac{\pi i}{K_p K'_p \,|\omega|}. \tag{A5}$$

Equation (22) is recovered upon defining the parallel scale of K as $L_K = K_p/K'_p$ where K_p is K evaluated at the location of the pole. [Here, we employ the definition of the pole, $\omega - \omega_{*e} = -\omega K_p^2$, to eliminate the numerator in the second term of Q in Eq. (A3).]

The global dispersion relation for the drift-Alfvén mode in this geometry is given by matching Eq. (17) for ψ in region one to Eq. (19) for ψ in region two, using the jump condition for $\nabla_{||}\psi$ given by Eqs. (21) and (22). The matching conditions at z = L are

$$A_2 = \cos k_{||1} L, \tag{A6}$$

$$i A_2 k_{||2} + k_{||1} \sin k_{||1} L = Q A_2. \tag{A7}$$

On eliminating A_2 and employing $x = k_{||1}L$ and $\xi = k_{||2}L$ Eq. (23) is immediately obtained. Equation (24) results from rewriting Eq. (18) in terms of x and ξ.

Appendix B: Analytic limits of the two-region model

The two region model is amenable to analytic solutions in many interesting limits. We shall consider a few cases here, initially neglecting the Q term. Its effect will be discussed subsequently.

In the small ξ limit, the tan x function can be expanded and x^2 can then be eliminated from Eq. (24) to obtain a quadratic equation for ξ

$$\xi - \xi_* = i K_0^2 \xi^2 \tag{B1}$$

If $\xi_* << 1$ we can further expand about $\xi = \xi_*$ (corresponding to $\omega = \omega_{*e}$) to obtain

$$\xi = \xi_* + i K_0^4 / \lambda^2. \tag{B2}$$

This solution corresponds to those obtained numerically by the BAL code in several important ways: i) Re ω is near ω_{*e} and $\gamma << \omega_{*e}$, ii) since x <<1, the mode is flat in region one (the region between the X-points). The solution is inadequate in that Eq. (B2) does not permit the determination of a fastest growing mode over K for fixed λ.

To remedy this, we consider the large ξ limit with the maximal ordering $\lambda \sim K^2$ <<1. In this limit, Eq. (23) can be solved to obtain $x = x_0 + x_1$ where $x_0 = \pi/2$ and $x_1 = -ix_0/\xi$. From this we obtain the dispersion relation

$$\xi = \xi_* + \frac{K_0^2 \xi^3}{x_0^2} + \frac{2iK_0^2 \xi^2}{x_0^2} \tag{B3}$$

where the last term is small when $\lambda \sim K_0^2$ but is required for instability in the sub-ordering limit $\lambda << K_0 << \lambda^{1/2}$. Here we concentrate on the regime $\lambda << 1$, which is usually the relevant one for experiments. Considering the sub-ordering first yields

$$\xi = \xi_* + \frac{K_0^5}{x_0^2 \lambda^3} + \frac{2iK_0^4}{x_0^2 \lambda^2}. \tag{B4}$$

This results in a growing mode very similar to that of Eq. (B2). Together, the two solutions cover the range $0 < K_0 << \lambda^{1/2}$. For larger K_0, the cubic term in ξ balances K_0/λ to yield

$$\xi = \left(-\frac{x_0^2}{\lambda K_0} \right)^{1/3} \tag{B5}$$

which has a growing root with Re $\xi > 0$. Detailed analysis of the full cubic equation, Eq. (B3), shows that the maximum growth rate, Im $\xi \sim \lambda^{-1/2}$, is achieved for $K_0 \sim 2\lambda^{1/2}$ but for slightly smaller $K \sim 0.8\,\lambda^{1/2}$ the growth rate drops rapidly to match onto Eq. (B4) where Im $\xi \sim 1$. The maximum growing mode has Re $\omega \sim \gamma \sim \omega_{*e} \sim (m_i/m_e)^{1/4} c_s/(LL_n)^{1/2}$ and is not flute-like in the central region since $x \sim \pi/2$ where $x = k_{\|1} L$. This limit is not seen in the BAL code, possibly because when the mode departs significantly from being flat in region one, the Born approximation is suspect. It is not surprising that the two-region model overestimates the growth rates that are obtained when the K profile is a smooth function of z or θ. This point is further expanded upon in Sec. IV B and in Fig. 8.

The above solutions are not dramatically affected by retaining the QL pole contributions. Treating $L_\|/L$ and L_K/L as order unity parameters, we note that Eq. (22) gives QL $\sim \xi^2$ which is therefore negligible in the small ξ solution of Eq. (B2). In the large ξ limit, the leading order solution of Eq. (23) for x remains $x \approx x_0 = \pi/2$, however the correction term x_1 now contains the new effects in QL. Thus the solution procedures for the large ξ solutions of Eqs. (B4) and (B5) are not modified in any essential way. The result is that Eq. (B5) is not modified to the order given and in Eq. (B4) the sound wave damping term arising from the pole residue now reduces the growth rate by competing with the drive term in Eq. (B4).

Appendix C: $\nu \to \infty$ limit of the power law model

In the $\nu \to \infty$ limit, the power law model for K given by Eq. (26) yields $K = K_0$ for $s\theta < 1$ and $K \to \infty$ for $s\theta > 1$. Thus, the solution of Eq. (25) in the two regions is

$$\psi = \begin{cases} \cos k\theta, & s\theta < 1 \\ A_2 \exp[i(s\theta - 1)\xi / s], & s\theta > 1 \end{cases} \tag{C1}$$

where

$$k = \frac{K_0 \xi}{\sqrt{1 + K_0^2 - \xi_* / \xi}} \tag{C2}$$

Matching ψ and $d\psi/d\theta$ at $s\theta = 1$ yields

$$k \tan(k / s) = -i\xi \tag{C3}$$

If we let $\tilde{x} = k / s$, $\tilde{\xi} = \xi / s$, $\tilde{K} = K_0 \Big/ \sqrt{1 + K_0^2}$, and $\tilde{\lambda} = \sqrt{1 + K_0^2}\ \lambda s$, then Eqs. (C2) and (C3) become

$$\tilde{x} \tan \tilde{x} = -i\tilde{\xi} \tag{C4}$$

$$\tilde{x}^2 \left(\tilde{\xi} - \frac{\tilde{K}}{\tilde{\lambda}} \right) = \tilde{K}^2 \tilde{\xi}^3 \tag{C5}$$

Equations (C4) and (C5) are precisely those of the two-region model.

References

[1] L.V. Mikhailovskii and A.B. Mikhailovskii, Sov. Phys. – JETP **18**, 1077 (1984).

[2] R.R. Dominguez, Nucl. Fusion **19**, 105 (1979).

[3] H.L. Berk and R.R. Dominguez, J. Plasma Phys. **17**, 31 (1977).

[4] A. Hasegawa and M. Wakatani, Phys. Rev. Lett. **50**, 682 (1983).

[5] P.N. Guzdar, L. Chen, P.K. Kaw and C. Oberman, Phys. Rev. Lett **40**, 1566 (1978).

[6] L. Chen, P.N. Guzdar, J.Y. Hsu, P.K. Kaw, C. Oberman, R. White, Nucl. Fusion **19**, 373 (1979).

[7] R.J. Hastie, K.W. Hesketh and J.B. Taylor, Nucl. Fusion **19**, 1223 (1979).

[8] J.W. Connor, J.B. Taylor and H.R. Wilson, Phys. Rev. Lett **70**, 1803 (1993).

[9] S. Briguglio, F. Romanelli, C.M. Bishop, J.W. Connor and R.J. Hastie, Phys. Fluids B **1**, 1449 (1989).

[10] S.J. Camargo, D. Biskamp and B.D. Scott, Phys. Plasmas **2**, 48 (1995).

[11] H. Sugama, M. Wakatani and A. Hasegawa, Phys. Fluids **31**, 1601 (1988).

[12] M. Wakatani, K. Watanabe, H. Sugama and A. Hasegawa, Phys. Fluids B **4**, 1754 (1992).

[13] A. Zeiler, D. Biskamp and J.F. Drake, Phys. Plasmas **3**, 3947 (1996).

[14] B.D. Scott, H. Biglari, P.W. Terry and P.H. Diamond, Phys. Fluids B **3**, 51 (1991).

[15] R. Kleiber, Phys. Plasmas **8**, 4090 (2001); and refs therein.

[16] O. Pogutse, Yu Igithanov, W. Kerner, G. Janeschitz, and J.G. Cordey, 24th EPS Conf. on Cont. Fusion and Plasma Phys (Berchesgarten, 1997) Vol. 21A, Part III, p. 1041; O. Pogutse and Yu Igithanov, Czechoslovak J. Phys **48** Suppl. S2 (1998) 39.

[17] J.W. Connor and O. Pogutse, Plasma Phys. Controlled Fusion **43**, 281 (2001).

[18] J.R. Myra, D.A. D'Ippolito, X.Q. Xu and R.H. Cohen, Phys. Plasmas **7**, 4622 (2000); J.R. Myra, D.A. D'Ippolito, X.Q. Xu and R.H. Cohen, Phys. Plasmas **7**, 2290 (2000).

[19] X.Q. Xu, R.H. Cohen, T.D. Rognlien and J.R. Myra, Phys. Plasmas **7**, 1951 (2000).

[20] M.N. Rosenbluth, N.A. Krall, and N. Rostoker, Nucl. Fusion Supplement Part 1, 143 (1962); M.N. Rosenbluth and A. Simon, Phys. Fluids **8**, 1300 (1965).

[21] B. Rogers, J.F. Drake and A. Zeiler, Phys. Rev. Lett **81**, 4396 (1998).

[22] P.N. Guzdar, R.G. Kleva, A. Das and P.K. Kaw, Phys. Rev. Lett **87**, 015001 (2001).

[23] R.J. Taylor, M.L. Brown, B.D. Fried, H. Grote et al., Phys. Rev. Lett. **63**, 2365 (1989).

[24] M. Peng, Phys. Plasmas **7**, 1681 (2000); S.M. Kaye et al., Fusion Technology **36**, 16 (1999).

[25] X.Q. Xu, W.M. Nevins, A. Mazurenko, M. Porkolab and D. Mossessian, Bull. Am. Phys. Soc. **46**, 186 (2001), paper KP1-021.

[26] I. Hutchinson, B. Boivin, F. Bombarda, P. Bonoli et al., Phys. Plasmas **1**, 1511 (1994).

Figure captions

1. Re and Im parts of ω (rad/s) vs. toroidal mode number n for the slab model dispersion relationship, showing the unstable coupling of the drift and Alfvén branches, and the low frequency sound wave. Plasma parameters are given in the text, $k_{||} = 1/R$ and $k_{\perp} = nB/RB_{\theta}$. The frequency of the sound wave has been artificially increased by a factor of 20 to make it visible on this plot.
2. BOUT comparisons of drift-wave instability in a) CCT and b) NSTX for similar plasma parameters. Shown are surface plots of $\delta n_{rms}/n_0$ vs. radial coordinate x and time t. The DW is stable in the circular flux surface geometry of CCT, while it is unstable in the divertor geometry of NSTX. Note the difference in scales on the vertical axis. In a) the plasma fluctuations remain at the small noise level where they were initialized.
3. Unstable spectrum, Im $\omega = \gamma$ (10^3 rad/s) vs. toroidal mode number n for a sample NSTX case illustrating DW instability in X-pt geometry. Curves are EM (solid), ES (blue) and EM with H = 0 (long-dashed and labeled "no Skin"). For these parameters (see text) the instability is driven mainly by the collisionless electron skin terms (electron inertia) and persists in the cold ion limit shown here.
4. Unstable spectrum, Im $\omega = \gamma$ (10^3 rad/s) vs. n for the base case, and a case with q doubled.
5. DW eigenfunction ψ vs. extended ballooning angle θ for the collisionless electrostatic model. X-points are located at $\theta = 0, 4$. Note the flat character of the mode between the X-points on the outboard side ($0 < \theta < 4$) and the outgoing wave feature that is evident at large $|\theta|$. Base case plasma parameters are employed and the mode shown is for n = 32 and ballooning parameter $\theta_0 = 2$.

6. Unstable spectrum, $\gamma = \mathrm{Im}\ \omega\ (10^3$ rad/s) vs. n for the X-point geometry case (X-pt), circular flux surface case (circle), circle case with X-pt $K(\theta)$ profile (K_x), and circle case with X-pt Jacobian (J_x). Only the circle case is stable.
7. a) Comparison of $K(\theta)$ profiles for an NSTX double null case (solid) and two power law forms: circular geometry: $s = 2$, $\nu = 2$ (long dashed), and best fit to NSTX: $s = 0.6$, $\nu = 20$ (short dashed). b) L/L_K comparisons for the same cases. The damping from the pole contribution is proportional to the inverse quantity L_K/L. When the pole is near the X-points at $\theta = 0, 4$ the damping is greatly reduced compared to the circular geometry case.
8. Dimensionless growth rate Im ξ vs. profile steepness ν for the case $K_0 = 0.4$, $\lambda = 0.3$ and $s = 0.3$. Note that $\nu = 2$ is stable (circular limit) and that $\nu \rightarrow \infty$ asymptotes to the two-region model shown by the dashed line.
9. Eigenfunctions $\phi(\theta)$ from the MBAL code for a nearly stable case without the sound wave (a) and with the sound wave (b). Retention of sound wave propagation resolves the singularity and leads to outgoing sound wave propagation but the growth rate is not changed significantly.

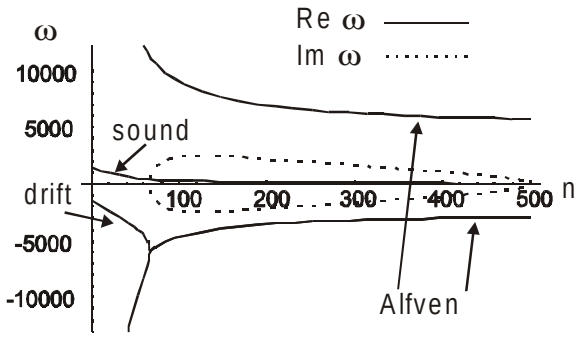

Fig. 1. Re and Im parts of ω (rad/s) vs. toroidal mode number n for the slab model dispersion relationship, showing the unstable coupling of the drift and Alfvén branches, and the low frequency sound wave. Plasma parameters are given in the text, $k_{||} = 1/R$ and $k_{\perp} = nB/RB_{\theta}$. The frequency of the sound wave has been artificially increased by a factor of 20 to make it visible on this plot.

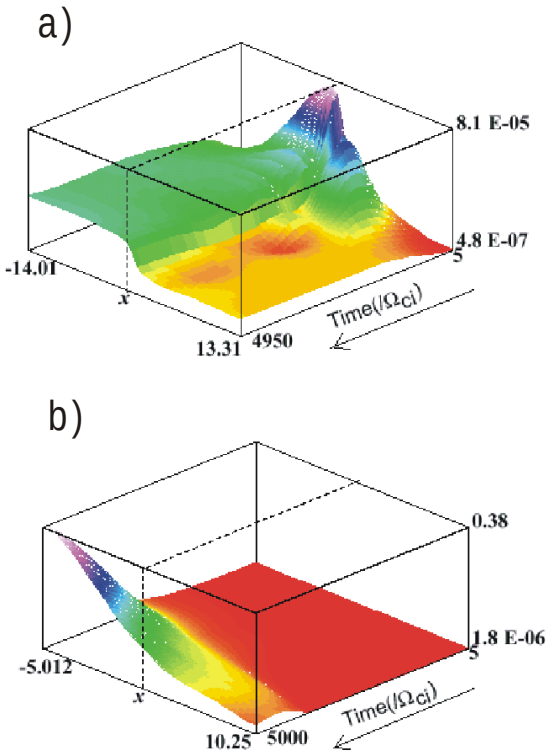

Fig. 2. BOUT comparisons of drift-wave instability in a) CCT and b) NSTX for similar plasma parameters. Shown are surface plots of $\delta n_{rms}/n_0$ vs. radial coordinate x and time t. The DW is stable in the circular flux surface geometry of CCT, while it is unstable in the divertor geometry of NSTX. Note the difference in scales on the vertical axis. In a) the plasma fluctuations remain at the small noise level where they were initialized.

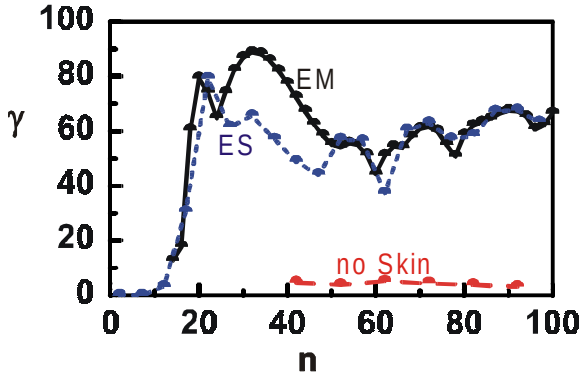

Fig. 3. Unstable spectrum, Im $\omega = \gamma$ (10^3 rad/s) vs. toroidal mode number n for a sample NSTX case illustrating DW instability in X-pt geometry. Curves are EM (solid), ES (blue) and EM with H = 0 (long-dashed and labeled "no Skin"). For these parameters (see text) the instability is driven mainly by the collisionless electron skin terms (electron inertia) and persists in the cold ion limit shown here.

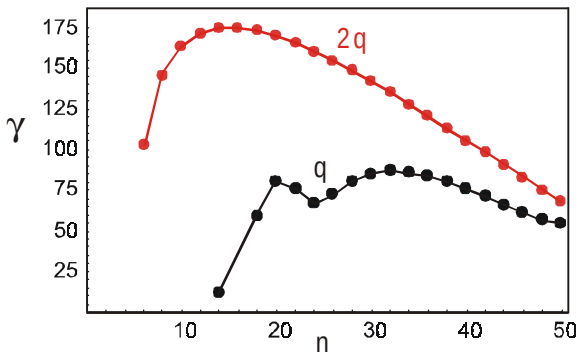

Fig. 4. Unstable spectrum, Im $\omega = \gamma$ (10^3 rad/s) vs. n for the base case, and a case with q doubled.

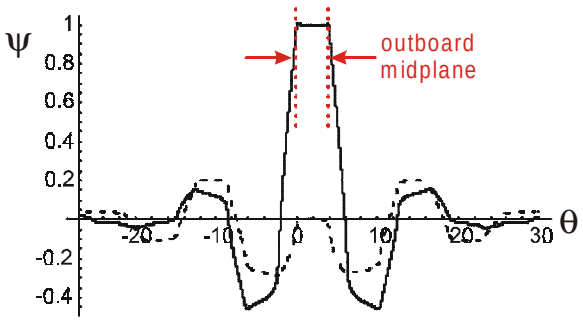

Fig. 5. DW eigenfunction ψ vs. extended ballooning angle θ for the collisionless electrostatic model. X-points are located at $\theta = 0, 4$. Note the flat character of the mode between the X-points on the outboard side ($0 < \theta < 4$) and the outgoing wave feature that is evident at large $|\theta|$. Base case plasma parameters are employed and the mode shown is for n = 32 and ballooning parameter $\theta_0 = 2$.

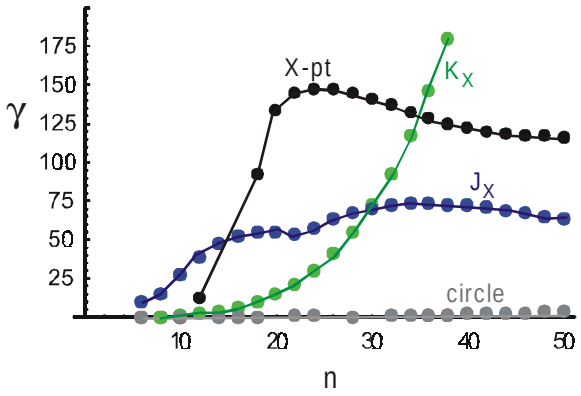

Fig. 6. Unstable spectrum, γ = Im ω (10^3 rad/s) vs. n for the X-point geometry case (X-pt), circular flux surface case (circle), circle case with X-pt K(θ) profile (K_x), and circle case with X-pt Jacobian (J_x). Only the circle case is stable.

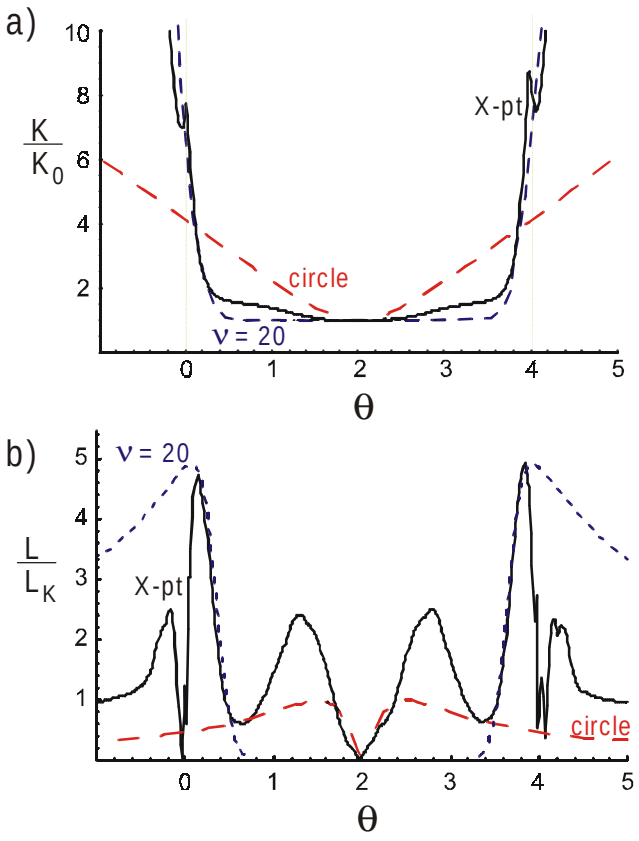

Fig. 7. a) Comparison of K(θ) profiles for an NSTX double null case (solid) and two power law forms: circular geometry: s = 2, ν = 2 (long dashed), and best fit to NSTX: s = 0.6, ν = 20 (short dashed). b) L/L_K comparisons for the same cases. The damping from the pole contribution is proportional to the inverse quantity L_K/L. When the pole is near the X-points at θ = 0, 4 the damping is greatly reduced compared to the circular geometry case.

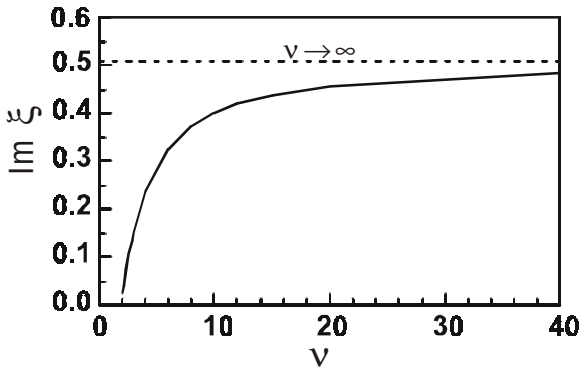

Fig. 8. Dimensionless growth rate Im ξ vs. profile steepness ν for the case $K_0 = 0.4$, $\lambda = 0.3$ and $s = 0.3$. Note that $\nu = 2$ is stable (circular limit) and that $\nu \rightarrow \infty$ asymptotes to the two-region model shown by the dashed line.

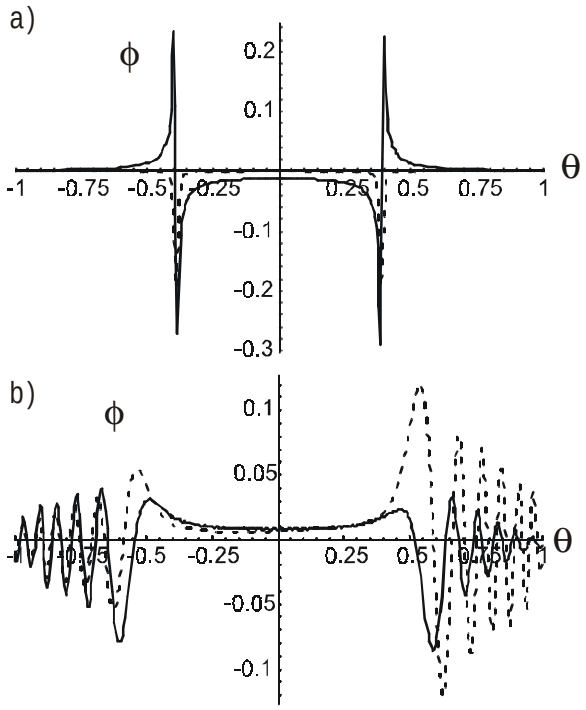

Fig. 9. Eigenfunctions $\phi(\theta)$ from the MBAL code for a nearly stable case without the sound wave (a) and with the sound wave (b). Retention of sound wave propagation resolves the singularity and leads to outgoing sound wave propagation but the growth rate is not changed significantly.